J. Appl. Comput. Mech., xx(x) (2026) 1-17
DOI: 10.22055/jacm.2026.49171.5779

ISSN: 2383-4536
jacm.scu.ac.ir

Shahid Chamran University of Ahvaz

Journal of Applied and Computational Mechanics

Research Paper

Three-Dimensional Numerical Simulation of Aircraft Wing Ice Accretion Using an Eulerian Droplet Model with Runback Water Distribution

Bangtuo Yu[1,2], Lifen Zhang[1], Chengxin Zhou[1], Yaguo Lyu[1], Zhengang Liu[1]

[1] Department of Power and Energy, Northwestern Polytechnical University, 1 Dongxiang Road, Xi'an, 710129, China,
Email: zhanglifen@nwpu.edu.cn (L.Z.); 381440678@qq.com (C.Z.); yglu@nwpu.edu.cn (Y.L.); zgliu@nwpu.edu.cn (Z.L.)

[2] Xi'an Precision Machinery Research Institute Kunming Branch, Kunming, 650000, China, Email: ybtuo@mail.nwpu.edu.cn

Received February 16 2026; Revised April 18 2026; Accepted for publication April 24 2026.
✉ Corresponding author: L. Zhang (zhanglifen@nwpu.edu.cn)

Abstract. Accurate simulation of three-dimensional ice accretion on aircraft wings remains challenging because droplet impingement, runback water transport, and ice-shape reconstruction are strongly coupled over complex surfaces. To address this issue, a three-dimensional numerical icing framework is developed on the Fluent platform. The local water collection coefficient is calculated using an Eulerian droplet model solved through the user-defined scalar (UDS) approach, in which impingement and non-impingement regions are distinguished according to the droplet velocity and wall-normal vector. A diffusion term is introduced to improve numerical robustness. Based on the Messinger thermodynamic icing model, a runback water treatment for unstructured surface grids is established, together with an area-weighted ice-shape reconstruction and mesh-deformation method for multi-step three-dimensional icing simulation. The method is validated using the NACA0012 straight wing and the MS-317 swept wing under representative icing conditions. For droplet impingement, the predicted local water collection coefficient agrees well with the reference data, with a relative error of less than 1.6% near the leading edge for the NACA0012 case. For the NACA0012 airfoil, the maximum ice-thickness error is 1.32% under rime ice conditions, while the deviation in icing limit is about 2.3% under glaze ice conditions. For the MS-317 swept wing, the maximum ice-thickness error is about 8.4% under rime ice conditions and 1.87% under glaze ice conditions at 1164 s, although the icing-limit deviation remains about 33%. Overall, the proposed framework shows good predictive capability, whereas icing-limit prediction under long-duration glaze ice conditions still requires improvement.

Keywords: Runback water, Eulerian two-phase flow, 3-D icing simulation, Ice-shape reconstruction, Multi-step simulation.

1. Introduction

Icing is one of the significant factors threatening aircraft flight safety. When an aircraft flies through clouds containing supercooled water droplets, icing can occur on various parts of the aircraft surface, such as the wings, windshields, and engine intakes and blades [1, 2]. Ice accumulation on the aircraft surface alters the aerodynamic configuration, reducing aerodynamic performance and affecting the aircraft's stability and maneuverability [3]. When ice reaches a certain thickness, it may shed and potentially damage compressor blades, posing a severe risk to flight safety [4]. Currently, there are three main methods for studying aircraft icing: flight tests, wind tunnel experiments, and numerical simulations. Due to the unpredictability of natural conditions, flight tests can be risky but yield the most reliable results [5]; icing wind tunnel experiments are relatively lower in cost and more feasible than flight tests, though they often require scaling down the research object due to size limitations of the wind tunnel [6]; Compared with flight tests and wind tunnel experiments, numerical simulation offers advantages such as shorter research cycles, lower cost, and greater flexibility [7], making it an important approach for studying aircraft icing. Currently, widely used icing software includes NASA's LEWICE [8, 9], DRA's TRAJICE [5], ONERA's icing program [10], and FENSAP-ICE [2, 11].

Numerical simulation of icing typically involves four steps: (1) First, solve the airflow field; (2) After convergence, solve the water droplet control equations to obtain the local water collection coefficient; (3) Then, select an appropriate icing model to solve for icing characteristics and determine the ice thickness; (4) Finally, construct the ice shape based on the computed results. In solving the airflow field, CFD methods are mainly used to solve the Navier-Stokes equations. The calculation of the local water collection coefficient primarily uses the Lagrangian method and the Eulerian method. The Lagrangian method calculates collection efficiency by tracking the trajectories of multiple droplets released from different initial positions in the far field [5]; The Eulerian method treats water droplets as a continuous phase, introducing a droplet volume fraction to represent the proportion of supercooled droplets in the air-water two-phase flow field. By solving the droplet phase control equations, the impact area and amount of water droplets on the object's surface are obtained [12]. Given that the Eulerian method has significant advantages over the Lagrangian method when applied to three-dimensional complex geometries [13], this paper uses the Eulerian method for calculating the local water collection coefficient.

Currently, most icing software is based on models derived from the classical Messinger icing model [14]. Unlike two-dimensional icing, the flow direction of liquid water in three-dimensional icing is no longer strictly aligned with the streamlines, and the overflow and redistribution of unfrozen water therefore need to be considered. Al-Khalil et al. [15] treated the water film as a rectangular layer, maintained the humidity factor, and calculated the film thickness through mass conservation, thereby reducing the three-dimensional problem to a simplified two-dimensional treatment and significantly lowering the numerical complexity and computational cost. Myers [16] proposed a water-film flow model applicable to arbitrary three-dimensional surfaces. This model accounts for heat conduction between the water film and ice layer during glaze-ice growth, as well as the effects of air shear stress, air-pressure gradient, and surface characteristics on water-film motion. Rothmayer et al. [17] characterized water-film flow according to the ratio of film thickness to boundary-layer thickness and the associated inertial effects. Bourgault et al. [10] introduced a shallow-water model in FENSAP-ICE to better represent the effects of pressure gradient and surface tension on water-film flow, while ensuring that no liquid-water motion occurs below the freezing point. Yanxia et al. [18] investigated the influence of gravity, aerodynamic shear stress, and surface tension on water-film flow, and showed that airflow velocity is a key factor governing runback water, with higher velocity leading to larger shear stress and a thinner water film. Dong et al. [19] developed a mathematical model to predict the shape and size of water-film rupture and analyzed the effects of inflow velocity and temperature on film thickness and morphology. Zheng et al. [20] employed the volume-of-fluid (VOF) method to study water-film flow on anti-icing surfaces, taking into account the effects of surface tension and contact angle. More recent studies have further highlighted the strong dependence of ice accretion behavior on icing conditions and operating environments. Gao et al. [21] experimentally investigated the dynamic evolution of ice accretion under various icing conditions, while Wang et al. [22] combined experimental and numerical approaches to analyze icing characteristics under operating conditions, providing further insight into the distribution and growth behavior of ice accretion. In addition, Yang et al. [23] examined the influence of different turbulence models on ice-accretion simulation and further optimized the computational approach for three-dimensional icing analysis.

In terms of ice-shape reconstruction, Hospers et al. [24] first identified the stagnation point and numbered each control volume along the streamlines. By tracking the surface flow direction, they determined the sequence of ice growth on the wall. Donizetti et al. [25] proposed an automatic time-step selection method based on a local growth-limiting factor to improve the stability of multi-step ice-accretion simulations and to avoid non-physical ice shapes caused by excessive geometric deformation. Yang et al. [26] reconstructed the ice shape by assigning ice thickness to surface nodes and deforming the profile accordingly. Bornhoft et al. [27] demonstrated the effectiveness of wall-modeled large-eddy simulation in resolving the complex aerodynamic effects of iced airfoils and emphasized the importance of accurate geometric representation of the ice shape and surface roughness. Tu et al. [28] investigated the effects of different coatings on delaying ice accretion and showed that the hydrophobicity of anti-icing coatings can effectively suppress ice formation.

In summary, although considerable progress has been made in droplet impingement simulation, thermodynamic icing modeling, and ice-shape reconstruction, several practical issues still remain in three-dimensional wing icing simulation. First, an Eulerian droplet impingement method that can be conveniently implemented in Fluent is still needed for complex three-dimensional wing configurations. Second, for three-dimensional icing on unstructured surface grids, a simple and practical runback water distribution strategy is required, especially one that does not rely on explicit stagnation-point detection. Third, in existing ice-shape reconstruction methods, the nodal ice height is typically obtained by averaging the ice thicknesses of adjacent surface cells.

To address these issues, the present study develops a three-dimensional numerical icing framework on the Fluent platform. An Eulerian droplet model solved through the UDS approach is used to calculate the local water collection coefficient, a runback water distribution method for unstructured surface grids is established based on the Messinger thermodynamic icing model, and an area-weighted ice-shape reconstruction and mesh-deformation procedure is implemented using Fluent's dynamic mesh capability.

In terms of droplet motion, an Eulerian droplet impingement model is established and solved using Fluent's user-defined scalar (UDS) approach. Impingement and non-impingement regions are distinguished according to the droplet velocity and the wall-normal vector. To alleviate the numerical divergence that may arise in solving the droplet governing equations with the Eulerian method, a numerical diffusion term is introduced to improve the robustness of the calculation.

In terms of icing simulation, the classical Messinger icing model is extended by incorporating runback water effects. A method is developed to determine the overflow direction of unfrozen water on unstructured surface grids, together with a mass-flux distribution strategy based on the angle between the air velocity vector and the normal vectors of grid edges. In addition, a three-dimensional ice-growth and reconstruction method is developed using Fluent's dynamic mesh module, in which the influence of local grid area on ice growth is taken into account. This framework enables multi-step three-dimensional icing simulation on complex wing surfaces.

2. Three-dimensional Eulerian Approach to Droplet Impingement Simulation

In this study, an Eulerian approach was employed to simulate the air-droplet two-phase flow. The external airflow was calculated using Fluent by solving the Navier-Stokes equations. The air phase influences the droplet phase through forces such as drag and turbulence effects. Under aircraft icing conditions, the volume fraction of the droplet phase is very small, typically on the order of 10^{-6}, which allows the assumption that the droplet phase has no effect on the air phase, leading to a one-way coupling [29]. Additionally, the density of the droplets is significantly higher than that of the surrounding air, and the droplet diameters are sufficiently small relative to the characteristic length of the flow field. Based on these considerations, the following reasonable assumptions are made:

(1) The droplet shape is assumed to be spherical, with no deformation or breakup occurring during its motion.
(2) There is no collision or coalescence between droplets, and no rebound or splashing occurs upon impact with the surface.
(3) Viscosity and pressure terms are neglected in the momentum equation of the droplet phase.
(4) No mass or heat transfer occurs between the droplets and the surrounding air.
(5) Only drag and gravity forces are considered acting on the droplets.

2.1. Governing equations for droplet phase

Based on the above analysis and assumptions, the continuity equation and momentum equation for the droplet phase are derived as follows:

$$\frac{\partial(\alpha\rho_d)}{\partial t} + \nabla\cdot(\rho_d\alpha\mathbf{u}_d) = 0 \tag{1}$$

$$\frac{\partial(\alpha\rho_d\mathbf{u}_d)}{\partial t} + \nabla(\alpha\rho_d\mathbf{u}_d\mathbf{u}_d) = \rho_d\alpha K(\mathbf{u}_a - \mathbf{u}_d) + \alpha\rho_d\mathbf{g} \tag{2}$$

In the formula, α represents the volume fraction of the droplets, ρ_d is the density of the supercooled droplets, $\mathbf{u}_d$ is the velocity vector of the droplets, $\mathbf{u}_a$ is the velocity vector of the air, $\mathbf{g}$ represents the gravitational acceleration, and K is the air-droplet momentum exchange coefficient, defined by Eq. (3):

$$K = \frac{18\mu_a f}{\rho_d D^2} \tag{3}$$

where f is the drag coefficient, μ_a is the dynamic viscosity of the air, D is the diameter of the supercooled droplets, and f is determined using the Schiller-Naumann model [30]:

$$f = \frac{C_D \mathrm{Re}}{24} \tag{4}$$

In Eq. (4), Re is the Reynolds number, where the characteristic velocity is the relative velocity, and C_D is the drag coefficient. The calculation formula is given as follows [30]:

$$\mathrm{Re} = \frac{\rho_a\,|\,\mathbf{u}_a - \mathbf{u}_d\,|\,D}{\mu_a} \tag{5}$$

$$C_D = \begin{cases} 24(1+0.15\mathrm{Re}^{0.687})/\mathrm{Re} & \mathrm{Re} \le 1000 \\ 0.44 & \mathrm{Re} > 1000 \end{cases} \tag{6}$$

To avoid the issue of infinite density jumps that can occur during droplet trajectory crossing as mentioned in reference [29], a numerical diffusion term has been introduced into the droplet governing equation, as shown in Eq. (7):

$$\frac{\partial(\alpha\rho_d)}{\partial t} + \nabla\cdot(\rho_d\alpha\boldsymbol{u}_d) = \Gamma\nabla^2(\rho_d\alpha) \tag{7}$$

The diffusion coefficient in this study is calculated using the method described in reference [31], which is based on the difference in droplet volume fraction between the current grid and the adjacent grids. The calculation formula for Γ is as follows:

$$\Gamma = a\times(e^b - 1) \tag{8}$$

where a is a proportionality factor, which is set to 0.001 in this study, and b is calculated using the following formula:

$$b = \max\{\frac{|a_P - a_{N_i}|}{\min\{a_P, a_{N_i}\}}, i = 0,1,2,\ldots k\} \tag{9}$$

In this equation, the subscript P denotes the current grid, while N_i indicates the surrounding adjacent grids, as shown in Fig. 1.

The value of b represents the maximum relative difference in droplet volume fraction between the current grid and the surrounding grids. For regions where the droplet volume fraction α is normal, the value of b approaches 0, leading to a diffusion coefficient that also approaches 0.

Conversely, for regions where α is anomalous, as α increases, the value of b increases as well. The exponential function facilitates rapid mitigation of numerical singularities within these domains.

2.2. Solution of the droplet governing equations

The droplet phase governing equations in this study are solved using the Fluent User-Defined Scalar (UDS) module, which allows for the definition of additional scalar transport equations. For any scalar ϕ_k, it can be expressed as follows [26]:

$$\underbrace{\frac{\partial\rho\phi_k}{\partial t}}_{\text{unsteady term}} + \frac{\partial}{\partial x_i}\left(\underbrace{\rho u_i\phi_k}_{\text{flux term}} - \underbrace{\Gamma_k(\partial\phi_k/\partial x_i)}_{\text{diffusivity term}}\right) = \underbrace{S_{\phi_k}}_{\text{source term}} \tag{10}$$

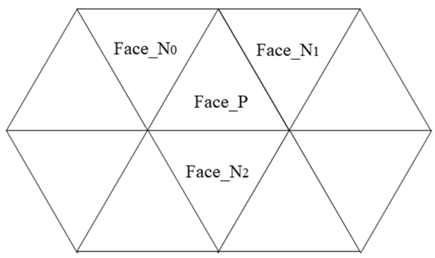

Fig. 1. Schematic of the unstructured grid.

Table 1. Applied UDF macros and their meanings.

UDF Macros	Meanings of UDF Macros
DEFINE_UDS_UNSTEADY	Defining the unsteady term in the droplet control equation
DEFINE_UDS_FLUX	Defining the advection term
DEFINE_DIFFUSIVITY	Defining the diffusion term
DEFINE_SOURCE	Defining the source term
DEFINE_PROFILE	Defining boundary conditions for droplet volume fraction and velocity at wall surfaces
DEFINE_ADJUST	Calculating local water collection coefficient and droplet impingement mass flow rate

In the formula, the terms are defined as follows: the **unsteady term** represents the transient component of the equation; the **flux term** indicates the convective component; the **diffusivity term** corresponds to the diffusion component of the transport equation; the **source term** represents the source term of the equation; and k denotes the number of user-defined scalars.

Based on the droplet phase governing Eq. (1) and (2), four scalars are defined: the droplet volume fraction α, and the droplet velocity components in the x, y, and z directions $u_{d,x}$, $u_{d,y}$, and $u_{d,z}$. To solve these scalars, the UDF macro functions applied to each term in the equations are listed in Table 1.

The detailed calculation process is as follows:

(1) In the Fluent solver, the unsteady term is decomposed into the source term **su** and the central coefficient term **apu** when calculating transient terms. Therefore, the discretization of the unsteady term in the mass conservation equation for droplets is as follows:

$$\text{unsteady term} = -\int \frac{\partial}{\partial t}(\rho_d \alpha) dV \approx -\left[\frac{(\rho_d\alpha)^n - (\rho_d\alpha)^{n-1}}{\Delta t}\right]\cdot \Delta V = \underbrace{-\frac{\rho_d \Delta V}{\Delta t}}_{\text{apu}}\alpha^n + \underbrace{\frac{\rho_d \Delta V}{\Delta t}}_{\text{su}}\alpha^{n-1} \tag{11}$$

For the momentum conservation equation, **apu** and **su** are defined as follows:

$$\text{unsteady term} = \underbrace{-\frac{(\rho_d\alpha)\Delta V}{\Delta t}}_{\text{apu}} u_d{}^n + \underbrace{\frac{(\rho_d\alpha)\Delta V}{\Delta t}}_{\text{su}} u_d{}^{n-1} \tag{12}$$

In the equation, u_d^n represents the components of droplet velocity in different directions, as shown in Eq. (13). After implementing the above formula in C-language, the values are returned to the Fluent solver using the DEFINE-UDS-UNSTEADY macro.

(2) The general form of the convective term in partial differential equations is represented as $\nabla\cdot(\psi\phi)$, where ψ is the vector field and ϕ is the user-defined scalar. The computation of the convective term requires returning the value of $\psi\cdot\mathbf{A}$ to Fluent, where $\mathbf{A}$ is the area vector of the grid. In the continuity equation for droplets, α denotes the user-defined scalar UDS0, and $\rho_d\mathbf{u}_d$ represents the vector field; therefore, the value to be returned is $\rho_d\mathbf{u}_d\cdot\mathbf{A}$.

For the momentum equation of droplets, Eq. (2) must first be decomposed into scalar form as follows:

$$\left.\begin{aligned}
\frac{\partial(\alpha\rho_d u_{d,x})}{\partial t} + \nabla\cdot(\rho_d\alpha u_{d,x}\mathbf{u}_d) &= \rho_d\alpha K(u_{a,x} - u_{d,x}) + \rho_d\alpha g_{d,x} \\
\frac{\partial(\alpha\rho_d u_{d,y})}{\partial t} + \nabla\cdot(\rho_d\alpha u_{d,y}\mathbf{u}_d) &= \rho_d\alpha K(u_{a,y} - u_{d,y}) + \rho_d\alpha g_{d,y} \\
\frac{\partial(\alpha\rho_d u_{d,z})}{\partial t} + \nabla\cdot(\rho_d\alpha u_{d,z}\mathbf{u}_d) &= \rho_d\alpha K(u_{a,z} - u_{d,z}) + \rho_d\alpha g_{d,z}
\end{aligned}\right\} \tag{13}$$

From the above equation, it is clear that the user-defined scalars for the three equations to be calculated are the magnitudes of the droplet velocities in the x, y, and z directions, denoted as $u_{d,x}$, $u_{d,y}$, and $u_{d,z}$, which are represented in the program as UDS1, UDS2, and UDS3, respectively. The vector field is represented as $\rho_d\alpha\mathbf{u}_d$, so the value to be returned is $\rho_d\alpha\mathbf{u}_d\cdot\mathbf{A}$.

In the DEFINE-UDS-FLUX macro function, the droplet volume fraction, droplet velocity, air velocity, and grid area normal vector are extracted for each grid cell. Then, the corresponding return values are calculated based on the different user-defined scalar indices.

(3) For the source term in the momentum equation, defined by the macro function DEFINE-SOURCE, the return value in the x direction is given by:

$$\rho_d\alpha K(u_{a,x} - u_{d,x}) + \rho_d\alpha g_{d,x} \tag{14}$$

The solution method for the three directions is consistent, only the component values need to be changed.

(4) The diffusion term is defined within the DEFINE-DIFFUSIVITY macro, with the return value set as $\rho_d\Gamma$.

2.3. Boundary condition analysis

The boundary conditions for droplet flow include three types: inlet, outlet, and wall boundaries. For the far-field inlet boundary, the droplets and air are undisturbed, and the relative velocity is zero. Therefore, the droplet velocity at the far-field is equal to the velocity of the air boundary. The droplet volume fraction α_∞ at the far-field is calculated according to the following equation:

$$\alpha_\infty = \frac{\text{LWC}}{\rho_d} \tag{15}$$

where LWC is the liquid water content in the incoming air. For the outflow boundary, the droplet volume fraction and velocity can be assigned using the results from the adjacent grid cells [29]. Regarding the wall boundary condition, it is necessary to determine whether the droplets impact the surface.

The relationship between the droplet velocity $\mathbf{u}_d$ and the wall normal $\mathbf{n}$ is illustrated in Fig. 2. For the boundary grid, the Fluent normal vector always points outward from the computational domain.

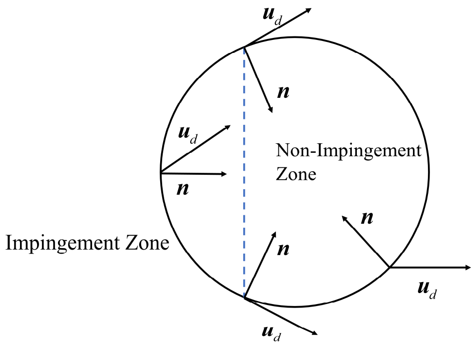

Fig. 2. Schematic of wall normal vector and droplet velocity.

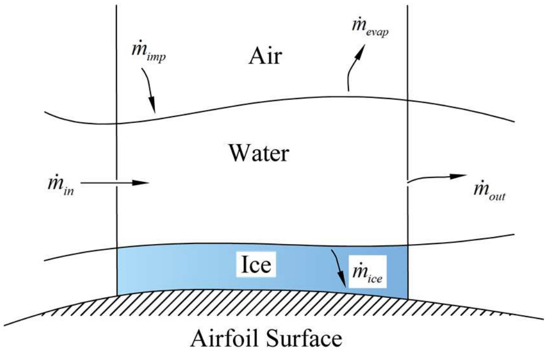

Fig. 3. Mass transfer within the control unit.

The method for distinguishing between the droplet impact zone and non-impact zone in this study is based on the dot product of the droplet velocity $\mathbf{u}_d$ and the wall mesh normal vector $\mathbf{n}$.

If $\mathbf{u}_d \cdot \mathbf{n} > 0$, it indicates that the droplet collides with the wall, and these droplets should be excluded from the computational domain. In this impact zone, the droplet volume fraction and velocity at the wall are set to the values from the adjacent incoming mesh.

Conversely, if $\mathbf{u}_d \cdot \mathbf{n} < 0$, it indicates that the wall mesh does not collide with the droplet, designating it as the non-impact zone. In this region, the wall droplet volume fraction is set to zero, and the droplet velocity follows a no-slip boundary condition, $\mathbf{u}_d \cdot \mathbf{n} = 0$, ensuring that wall information does not interfere with the results in the computational area.

To avoid numerical singularities and enhance computational stability, a small value is used to replace the droplet volume fraction in the non-impact zone, which is set to 10^{-13} in this study.

Boundary condition determination is implemented using the DEFINE-PROFILE macro, which is added to the wall surface in the program.

2.4. Droplet collection efficiency calculation

In the calculation of ice formation, it is necessary to determine the distribution of water impacting the wing surface by calculating the local collection coefficient. The local collection coefficient, denoted as β, is the ratio of the actual amount of water collected by an infinitesimal surface to the maximum amount that could potentially be collected. This coefficient is a crucial parameter influencing the final amount of ice accumulation, as calculated by the following formula [30]:

$$\beta = \frac{\alpha}{\alpha_\infty} \cdot \frac{\mathbf{u}_d \cdot \mathbf{n}}{|\mathbf{u}_{d,\infty}|} \tag{16}$$

In the equation, the subscript ∞ indicates the position where the incoming flow is undisturbed, while $\mathbf{n}$ represents the unit normal vector of the impacting surface mesh.

3. Three-dimensional Ice Accretion Model

Based on the two-dimensional icing model proposed by Messinger [13], this study establishes a three-dimensional ice accretion model that considers the effects of runback water. Additionally, a distribution scheme for the overflow flow on unstructured grid surface elements is developed, along with an iterative solution method tailored for this model.

3.1. Mass conservation in the control unit

The mass conservation schematic of the control unit is illustrated in Fig. 3. In the icing calculations, the control volume consists of each grid cell on the icing surface.

For the control volume on the icing surface, the mass conservation equation is expressed as:

$$\dot{m}_{imp} + \sum \dot{m}_{in} = \sum \dot{m}_{out} + \dot{m}_{evap} + \dot{m}_{ice} \tag{17}$$

where $\dot{m}_{imp}$ represents the mass flow rate of water impingement, $\sum \dot{m}_{in}$ is the total inflow runback water mass flow rate, $\sum \dot{m}_{out}$ is the outflow runback water mass flow rate of the current control volume, $\dot{m}_{evap}$ is the evaporative water mass flow rate, and $\dot{m}_{ice}$ is the frozen water mass flow rate. All terms are measured in kg/s.

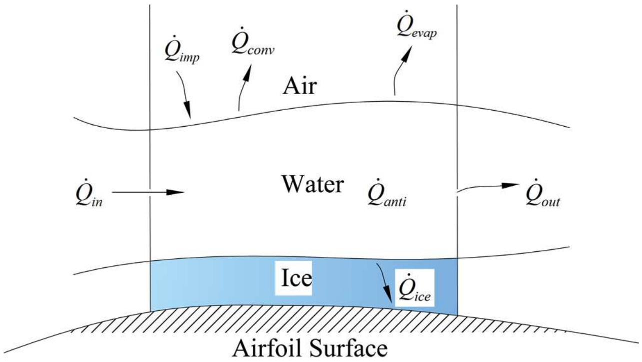

Fig. 4. Energy transfer within the control unit.

To describe the icing condition, a freezing coefficient f is introduced, defined as the ratio of the actual amount of ice formed in the control volume to the actual water collected over a unit time. The formula for calculating f is as follows:

$$f = \frac{\dot{m}_{ice}}{\sum \dot{m}_{in} + \dot{m}_{imp}} \tag{18}$$

From the definition of f, it is evident that its value ranges from $0 \leq f \leq 1$. When $f = 1$, all the water in the control volume freezes, resulting in rime ice, with no overflow occurring. When $0 < f < 1$, part of the water in the control volume freezes while the rest overflows into adjacent grid cells, indicating the presence of glaze ice. When $f = 0$, it signifies that none of the water entering the control volume has frozen, and only overflow occurs.

3.2. Energy conservation in the control unit

The energy balance diagram within the control unit is shown in Fig. 4. The corresponding energy conservation equation is as follows:

$$\sum \dot{Q}_{in} + \dot{Q}_{imp} + \dot{Q}_{ice} + \dot{Q}_{anti} = \dot{Q}_{evap} + \sum \dot{Q}_{out} + \dot{Q}_{conv} \tag{19}$$

where $\sum \dot{Q}_{in}$ represents the stagnation enthalpy of the water film combining the static enthalpy and kinetic energy flowing into the control volume. The stagnation enthalpy $\dot{Q}_{imp}$ is carried by impingement water flowing into the control volume. $\dot{Q}_{ice}$ consists of the latent heat released by ice accretion and the static enthalpy carried by the frozen water flowing out the control volume. $\dot{Q}_{anti}$ refers to the anti-icing heat flux, which is generally set to zero during freezing calculations due to the adiabatic treatment of the wall. $\dot{Q}_{evap}$ is the stagnation enthalpy carried by evaporated water out of the control volume. The stagnation enthalpy $\sum \dot{Q}_{out}$ is carried by water film flowing out the control volume, and $\dot{Q}_{conv}$ is the heat transfer due to convection. All units are in watts (W).

The specific calculation formulas for each term in the equation can be found in [26, 31]. The following sections will provide a detailed explanation of the criteria for determining the flow of runback water and its distribution method used in this study.

3.3. Distribution of runback water

The distribution of runback water presents a significant challenge in three-dimensional icing calculations. In two-dimensional icing computations, the wall grid typically has only one inlet and one outlet. However, three-dimensional icing surfaces often feature multiple inlets and outlets for water droplets. Determining the runback water direction and volume for each grid cell is central to solving the thermodynamic model for three-dimensional icing presented in this study.

For the current control volume, assume that all unfrozen water from the adjacent grids flows out, and the inflow amount $\dot{m}_{in,N}$ for each edge of the current grid equals the outflow from the neighboring control volume through edge N. By summing the inflow amounts for each edge, we obtain $\sum \dot{m}_{in}$. Therefore, the variables to be solved are the ice mass per unit time $\dot{m}_{ice}$, the outflow mass flow rate $\sum \dot{m}_{out}$, and the equilibrium temperature of the icing surface T_S.

From the definition of the freezing coefficient f, we have:

(1) If $f = 1$, it indicates that all supercooled water droplets impacting the wall have completely frozen, resulting in an outflow $\sum \dot{m}_{out} = 0$. The mass flux of ice increment is equal to the mass flow rate of the impacting water droplets plus the mass flow rate entering from adjacent control volumes. This can be calculated using the following equation:

$$\dot{m}_{ice} = \dot{m}_{imp} + \sum \dot{m}_{in} \tag{20}$$

At this point, it is only necessary to solve for the equilibrium temperature of the ice surface based on the principle of energy conservation.

(2) If $f = 0$, it indicates that no water droplets have frozen, resulting in an ice increment flux $\dot{m}_{ice} = 0$. The outflow $\sum \dot{m}_{out}$ can be calculated using the following equation:

$$\sum \dot{m}_{out} = \dot{m}_{imp} + \sum \dot{m}_{in} - \dot{m}_{evap} \tag{21}$$

Substituting $\dot{m}_{ice} = 0$ and the value of $\sum \dot{m}_{out}$ into the energy conservation equation yields the calculation of the ice surface temperature T_s.

(3) If $0 < f < 1$, indicating a mixture of ice and water, then $T_s = T_0$, where T_0 is the reference temperature, set at 273.15 K. In this case, $\dot{m}_{ice}$ can be obtained through the energy conservation equation, while the total outflow mass flux $\sum \dot{m}_{out}$ is subsequently computed via the mass balance equation.

From the analysis above, it can be seen that although the two equations correspond to three unknowns, the constraint imposed by the freezing coefficient allows for the reduction of one unknown. Therefore, the equations are solvable.

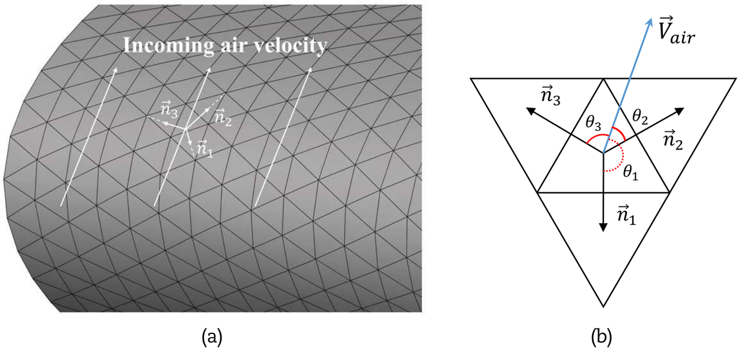

Fig. 5. Schematic of a 3D icing surface with unstructured mesh, (a) Diagram of the control volume at the icing surface, (b) Diagram of the angle betw een inlet velocity and the normal vectors of each grid edge.

However, the mass flow rates of water flowing into and out of each edge of the grid still need to be determined. The main driving force for the flow of unfrozen liquid water on the wing surface is the aerodynamic drag force. For unstructured grids, the distribution method proposed in this paper is as follows:

(1) The schematic of the control volume at the impact surface is shown in Fig. 5(a). An unstructured mesh is used to discretize the computational model, with triangular elements for the surface grid. Each mesh has three edges, where internal faces are adjacent to three neighboring grids, and boundary faces are adjacent to two. In this study, the airspeed $\mathbf{V}_{air}$ of the first layer of mesh near the icing surface is considered. By iterating through each point of the mesh and determining the coordinates, the unit normal vector $\mathbf{n}_i$ for each edge is calculated. The dot product of the inflow air velocity and the normal vector yields the value m_i, which is then used to determine whether water flows out.

$$m_i = \mathbf{V}_{air} \cdot \mathbf{n}_i \tag{22}$$

If $m_i > 0$, it indicates that water droplets will flow out of the i-th edge of the current mesh; if $m_i < 0$, it signifies that the outflow from the i-th edge of the current grid is zero. The normal vector $\mathbf{n}_i$ is defined as positive when pointing outward from the control volume.

(2) By cyclically traversing all the grids on the icing surface, each grid's inflow and outflow surfaces are identified and marked, stored in a structure for convenient access. Then, based on the values of m_i and the magnitude of the vector $\mathbf{V}_{air}$, the angle between the air velocity and the normal vector of each grid edge can be determined, as illustrated in Fig. 5(b). The outflow surfaces exhibit acute angles, while the inflow surfaces display obtuse angles.

(3) After calculating the total droplet outflow $\sum \dot{m}_{out}$ for each grid, the distribution is based on the number of outflow edges. If there is only one outflow edge, then $\sum \dot{m}_{out}$ flows entirely through that edge, with the outflow for the other edges being zero. If there are two outflow edges (for example, edges 2, and 3), the calculation is performed as follows:

$$\left.\begin{aligned} \dot{m}_{out,2} &= \frac{\theta_3}{\theta_2+\theta_3}\sum \dot{m}_{out} \\ \dot{m}_{out,3} &= \frac{\theta_2}{\theta_2+\theta_3}\sum \dot{m}_{out} \end{aligned}\right\} \tag{23}$$

It is assumed that the smaller the angle between the air velocity and the unit normal vector of the grid edge, the greater the likelihood that water droplets will flow out from that edge, resulting in a higher mass of overflow droplets. This is consistent with the actual flow behavior.

Additionally, during the grid partitioning process, local refinement of the grid at the ice surface is implemented to ensure good orthogonal quality. This approach aims to minimize the impact of grid edge lengths on runback water.

3.4. Solution methods for the 3D icing model

In two-dimensional icing calculations, it is common to identify stagnation points and then sequentially solve for each control unit from these points, dividing them into upper and lower sections [32]. However, in three-dimensional calculations, the flow direction of liquid water droplets within each grid is not fixed. A single grid can have multiple outflow surfaces simultaneously, and the overflow of supercooled droplets is no longer restricted to the streamline direction. Furthermore, in complex three-dimensional models, multiple stagnation points may exist at various locations, complicating the determination of the connection order of the grids near these points.

To address this, a method is proposed that involves cyclically calculating the control equations for water droplets on the grid surface, eliminating the need to identify the location of stagnation points. The specifics of this method are as follows:

(1) Let the total number of grid cells on the icing surface be N_{face}, and the iteration count be j. In the first iteration (when $j=0$), assume the mass of incoming water droplets for each grid cell, $\sum \dot{m}_{in}$, to be 0.

(2) For each grid cell, begin the calculations by assuming the icing condition to be glaze ice, with an equilibrium temperature $T_s = 273.15$ K. Calculate the evaporation mass flow rate of the droplets $\dot{m}_{evap}$ and the impact mass flow rate $\dot{m}_{imp}$. Then, solve for the frozen water mass flow rate $\dot{m}_{ice}$ using the energy equation and compute the total outflow mass flow rate $\sum \dot{m}_{out}$ based on mass conservation equation. After completing these calculations, determine the freezing coefficient f.

(3) If $0 < f < 1$, the assumption in step (2) holds. At this point, the control volume contains a mixture of ice and water, and the equilibrium temperature equals the freezing point (273.15 K). With known icing mass and total outflow mass, distribute the runback water based on the angle between the unit normal vector of each edge and the air velocity (Section 3.3), yielding the outflow water mass $\dot{m}_{out,i}$ from edge i. Simultaneously, ensure that the grid sharing edge i receives an inflow of $\dot{m}_{out,i}$.

(4) If $f \geq 1$, all supercooled droplets impacting the wall freeze entirely, resulting in an outflow mass $\sum \dot{m}_{out} = 0$. The icing mass is then recalculated using Eq. (20), and the surface equilibrium temperature T_s is determined from Eq. (19).

(5) If $f \leq 0$, it indicates that no water in the control volume has frozen, thus the icing mass $\dot{m}_{ice} = 0$. In this case, compare the

evaporation mass of the droplets with the total water mass in the control volume. If $\dot{m}_{evap} \geq \dot{m}_{imp} + \sum \dot{m}_{in}$, it implies all droplets have evaporated, leading to $\sum \dot{m}_{out} = 0$. Conversely, if $\dot{m}_{evap} < \dot{m}_{imp} + \sum \dot{m}_{in}$, calculate the total outflow mass $\sum \dot{m}_{out}$ using Eq. (21) and apply the method from Section 3.3 to distribute the runback water. Subsequently, substitute the icing mass and total outflow mass into the energy equation to solve for the surface equilibrium temperature T_s.

(6) After solving for all grid cells, proceed to the next iteration (j increments by 1). Starting from the second iteration, the total mass flow of incoming water for each grid cell equals the sum of the mass flow into all inflow surfaces: $\sum \dot{m}_{in} = \dot{m}_{in,0} + \dot{m}_{in,1} + \dot{m}_{in,2}$, where if edge i has no water inflow, $\dot{m}_{in,i} = 0$. Repeat steps (2) to (6) until $j = N_{face}$.

Once the iterative solving process is complete, all unknown variables for the icing surface will be clearly defined, allowing the calculation of icing thickness Δh for each grid cell based on the icing mass $\dot{m}_{ice}$, grid area A, and icing duration Δt:

$$\Delta h = \frac{\dot{m}_{ice} \cdot \Delta t}{\rho_{ice} A} \tag{24}$$

4. Ice Shape Construction Method

After solving the icing model to obtain the ice thickness for each grid on the icing surface, it is necessary to construct and update the ice shape. In existing studies, three-dimensional ice shapes are typically generated by reconstructing the surface nodes. The ice height at each point of the icing surface grid is the average of the ice heights of all grids containing that point [33]. The direction of ice growth is the sum of the normal vectors of the surrounding grids. Finally, based on the original coordinates of the points, the coordinate values are adjusted by adding the ice height multiplied by the corresponding components of the ice growth vector.

This paper builds on the aforementioned method by considering the influence of grid area on ice growth. Both the ice height and the direction of ice growth at the nodes are calculated using a weighted average based on the areas of adjacent grids.

The solution method for the icing model developed here is based on unstructured grids, hence the construction of the ice shape also targets unstructured grids. However, the number of neighboring grids around each point in an unstructured grid is uncertain, depending on the model and grid quality; the number of grids sharing the same point can be 5, 6, 7, etc.

Using the icing surface grid shown in Fig. 6 as an example, the point "node" has 6 neighboring grids. Each grid is denoted by its area A_i, the unit normal vector of the grid is represented as $\mathbf{n}_i$, and i denotes the grid's index.

After calculating the ice height h_i for each grid using Eq. (24), the ice height at the shared point "node" is computed using Eq. (25). In this example, $n = 6$. This means that the ice height at the shared point is obtained by summing the product of each grid's ice height and its area, averaging this sum, and then dividing by the average area.

$$h_{ice,node} = \frac{\dfrac{\sum_{i=1}^{n} h_i A_i}{n}}{\dfrac{\sum_{i=1}^{n} A_i}{n}} = \frac{\sum_{i=1}^{n} h_i A_i}{\sum_{i=1}^{n} A_i} \tag{25}$$

Once the ice height is determined, it is also necessary to obtain the direction of ice growth at the shared point "node." In this calculation, it is assumed that the ice grows along the wall normal, so the unit normal vector $\mathbf{n}_{node}$ at the shared point is calculated as follows:

$$\mathbf{n}_{node} = \frac{\sum_{i=1}^{n} A_i \mathbf{n}_i}{\left| \sum_{i=1}^{n} A_i \mathbf{n}_i \right|} \tag{26}$$

After obtaining the ice height $h_{ice,node}$ and the ice growth direction $\mathbf{n}_{node}(n_{node,x}, n_{node,y}, n_{node,z})$ at each point, the coordinates of the grid point after icing (x', y', z') are calculated using the following relationship:

$$node(x,y,z) \begin{cases} x' = x + h_{ice,node} \cdot n_{node,x} \\ y' = y + h_{ice,node} \cdot n_{node,y} \\ z' = z + h_{ice,node} \cdot n_{node,z} \end{cases} \tag{27}$$

Once the coordinates of the points after icing are computed, the geometric update of the icing surface is achieved using the dynamic mesh function module in Fluent. Custom functions are written within the framework of the DEFINE_GRID_MOTION macro, allowing for variable definitions and program coding. Upon completion of the calculations, the external shape of the iced component is obtained.

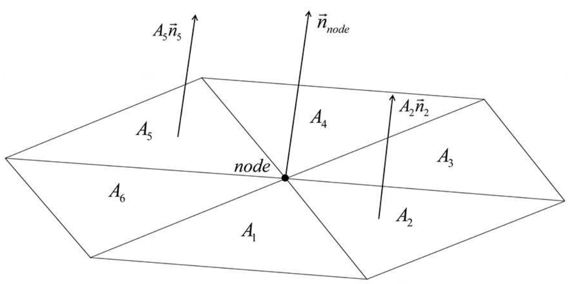

Fig. 6. Schematic of unstructured mesh with shared points.

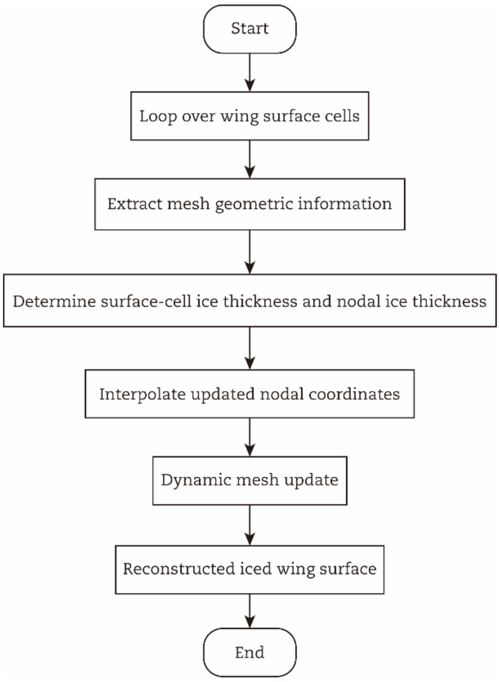

Fig. 7. Flowchart of ice-shape reconstruction and mesh deformation procedure.

The ice-shape reconstruction procedure is illustrated in Fig. 7 and can be summarized as follows:

(1) Characteristic parameters are extracted for each surface cell on the wing, including the cell index, centroid coordinates, cell area, and the coordinates of boundary nodes.

(2) Based on the coordinates of the boundary nodes, all neighboring cells surrounding each node are identified and their cell indices are stored for subsequent reconstruction.

(3) The local water collection coefficient obtained from the UDS-based droplet impingement calculation is introduced into the icing model, and the ice accretion thickness of each surface cell is obtained through iterative solution.

(4) The ice thickness is then interpolated to each surface node according to Eq. (25), and the local growth direction is determined according to Eq. (26).

(5) Finally, the updated coordinates of the wing surface nodes are calculated using Eq. (27) and assigned to the wing surface through the DEFINE_GRID_MOTION macro, so that the surface-node movement is completed and the iced wing geometry is reconstructed.

5. Calculation Results

5.1. Verification of the calculation method for local water collection coefficient

To validate the accuracy of the droplet impact characteristic calculation method proposed in this study, both a spherical surface and a three-dimensional NACA0012 airfoil were selected for computation, and the results were compared with those from existing literature [34, 35]. The diameter of the sphere is 15.04 cm, while the airfoil has a chord length of 0.914 m, a span of 1.828 m, and an angle of attack of 0 degrees. The inflow parameters are presented in Table 2.

The calculated results of the local water collection coefficient on the sphere surface are shown in Fig. 8. The local droplet collection coefficient cloud map from the sphere's surface indicates that the coefficient is significantly larger near the stagnation point, suggesting that more supercooled droplets impact the sphere's surface in this region. It clearly distinguishes between the impact and non-impact areas of the droplets.

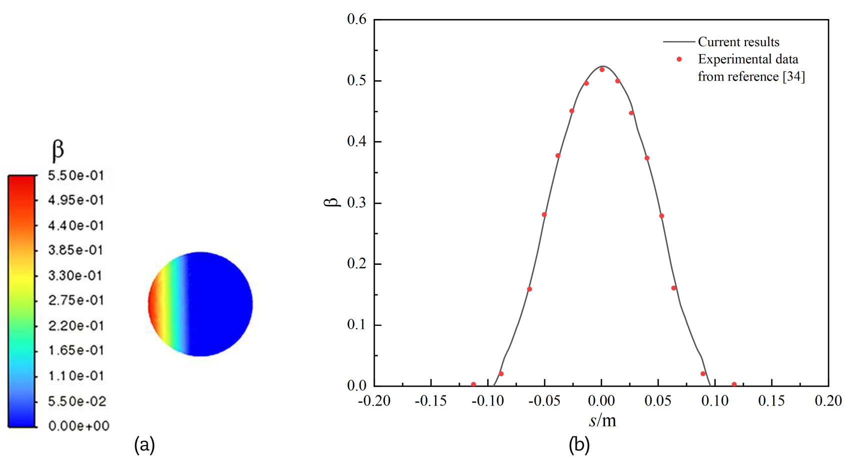

Fig. 8. Calculation results of local water collection coefficient on the sphere surface, (a) Contour of local water collection coefficient on the sphere surface, (b) Comparison results with experimental data.

Table 2. Inflow conditions for validation cases.

Parameters	Sphere	NACA0012 Airfoil
Liquid water content (LWC)	1 g/m^3	0.78 g/m^3
Incoming flow velocity	75 m/s	44.4 m/s
Ambient temperature	7 °C	-6.7 °C
Median volume diameter of water droplets (MVD)	18.6 μm	20 μm
Ambient pressure	95840 Pa	101325 Pa

Table 3. Calculation parameters.

Serial Number	Free stream temperature (°C)	Ice accretion time (s)	LWC (g/m^3)	MVD (μm)	Free stream velocity (m/s)	Free stream pressure (Pa)
1	-19.4	360	1.0	20	67.06	101300
2	-10	360	1.0	20	67.06	101300

Table 4. Grid independence analysis for the NACA0012 icing case.

Mesh level	Number of cells	Maximum ice thickness (mm)	Absolute relative change to next finer mesh (%)
G1	1.01M	30.12	8.20
G2	1.40M	27.65	2.93
G3	1.86M	26.84	0.45
G4	2.70M	26.72	-

A 2-D cross-section symmetrically extracted along the flow direction from the center of the sphere was unfolded along the arc length to analyze the variation of the local water collection coefficient with arc length. The results were compared with experimental findings from literature [34], as shown in Fig. 8(b). The computed results from this study align well with the distribution trends and magnitudes of the experimental data; however, the peak value of the droplet collection coefficient is slightly higher than the experimental values, while the calculated impact limit is lower than the experimental results.

The cloud map of the local droplet collection coefficient on the NACA0012 airfoil surface is shown in Fig. 9(a). From this figure, it is evident that droplet impacts are primarily concentrated near the stagnation point at the leading edge of the airfoil, with a maximum local droplet collection coefficient close to 0.6, which gradually decreases as one moves away from the stagnation point.

To quantitatively describe the differences between the results from this study and those from literature [35], the local droplet collection coefficient was extracted from the middle cross-section of the three-dimensional NACA0012 airfoil, unfolded along the airfoil chord. Negative values represent the lower surface of the airfoil, while positive values indicate the upper surface, with s/c = 0 corresponding to the leading edge of the airfoil. A comparison of these results with those from literature is presented in Fig. 9(b).

The results show that the calculations from this study are consistent with those from the literature, with a relative error of less than 1.6% for the local collection coefficient near the leading edge, although the calculated impact limit is slightly higher.

In summary, the calculations and validations of the local droplet collection coefficients for the 3-D sphere and the NACA0012 airfoil demonstrate that the droplet impact characterization method employed in this study is reliable. Therefore, the local droplet collection coefficients obtained using the UDS-based Eulerian method will be used in the subsequent ice accretion calculations.

5.2. Validation of Ice Shapes on NACA0012 Airfoil

The NACA0012 airfoil used for ice shape validation has a chord length of 0.5334 m and an angle of attack of 4°. The icing conditions are specified in Table 3.

The computational domain and mesh division are shown in Fig. 10. The airfoil is designated as a wall, with the far-field boundary set at a distance of 30 chord lengths to ensure adequate development of the incoming flow. Before the final simulations, a grid independence study was conducted for the NACA0012 rime-ice case. The inflow conditions used in this analysis were taken from Condition 1 in Table 3. Since the droplet impingement model had already been independently validated in Section 5.1, the maximum ice thickness was selected as the monitoring parameter in the present grid-sensitivity analysis. Four mesh levels with approximately 1.00, 1.40, 1.857, and 2.70 million cells were tested. The corresponding maximum ice thicknesses were 30.12, 27.65, 26.84, and 26.72 mm, respectively, as listed in Table 4. The absolute relative changes between two consecutive mesh levels were 8.20%, 2.93%, and 0.45%, respectively. Since the change between Grid 3 and Grid 4 was less than 1%, the mesh with 1,857,241 cells was considered sufficient to ensure mesh-independent results while maintaining acceptable computational cost.

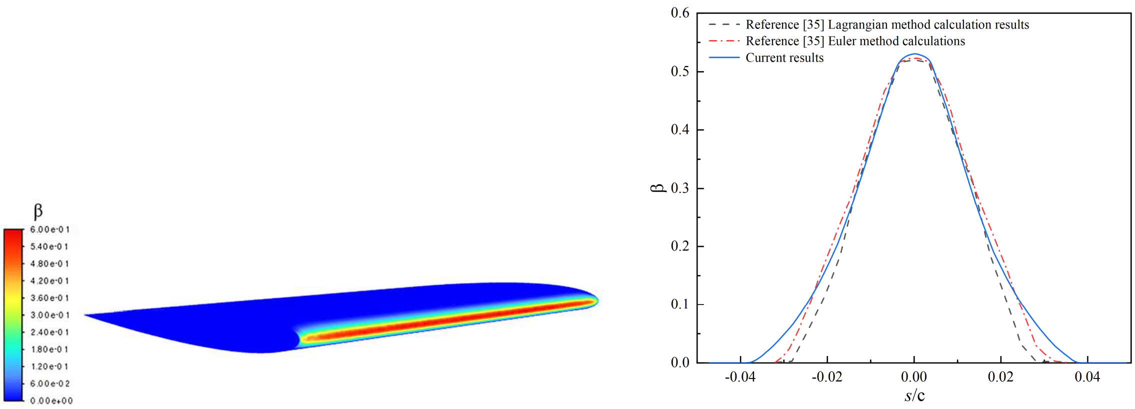

(a) (b)

Fig. 9. Calculation results of local water collection coefficient on the surface of NACA0012 airfoil, (a) Contour of the local water collection coefficient on the NACA0012 airfoil surface, (b) Results comparison.

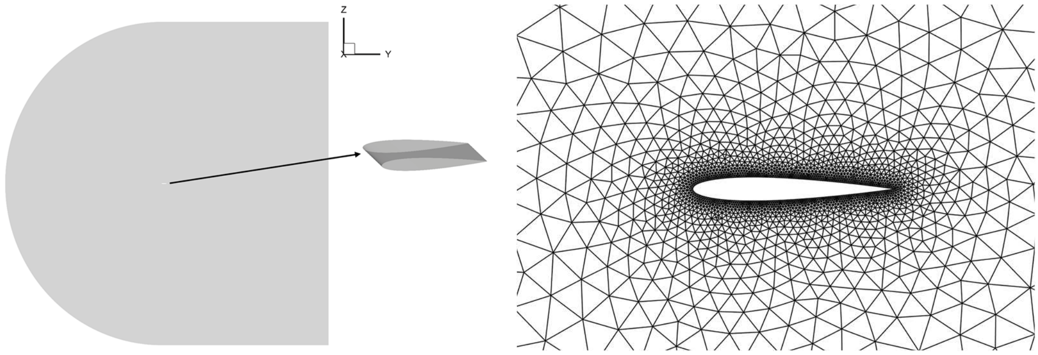

(a) (b)

Fig. 10. Computational domain and mesh division for NACA0012 icing validation, (a) Computational domain, (b) Mesh grid schematic.

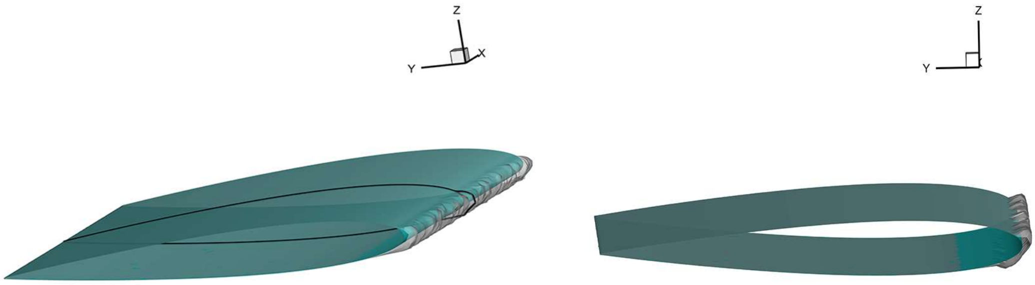

(a) (b)

Fig. 11. Icing conditions on airfoil surface at different temperatures, (a) Growth results of ice shapes at -19.4°C, (b) Growth results of ice shapes at -10°C.

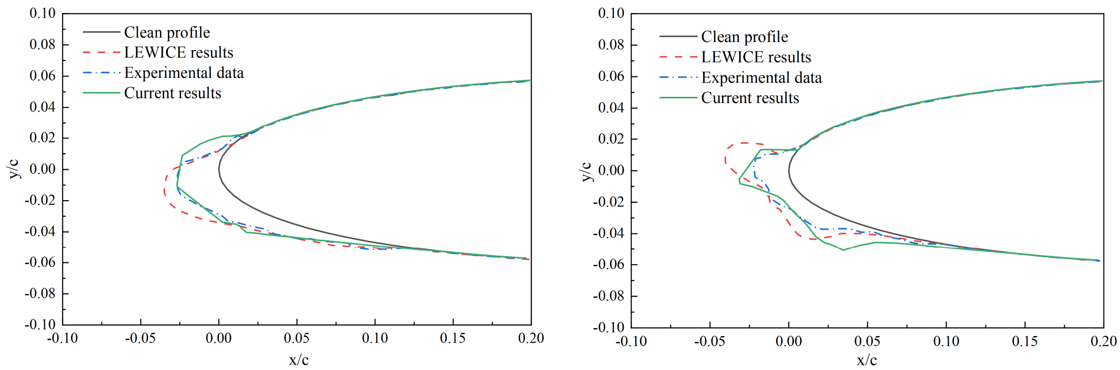

(a) (b)

Fig. 12. Comparison of ice shapes on NACA0012 airfoil surface at different temperatures, (a) Comparison results of ice shapes at -19.4°C, (b) Comparison results of ice shapes at -10°C.

Following convergence of the airflow field calculation, the UDS module was employed to compute the droplet impact characteristics. Once the droplet phase was solved, Fluent's Dynamic Mesh feature was utilized to implement a moving mesh for the airfoil, with the method selected as User-Defined. The flow field, droplet phase, and ice shape are updated every 120 seconds.

After the icing calculations were completed, the icing conditions on the airfoil surface at different temperatures are shown in Fig. 11. The green areas represent the smooth surface of the airfoil, while the transparent sections indicate the ice accumulated over a period of 6 minutes.

From Fig. 11, it can be observed that the shape of the airfoil changes after icing. The originally smooth airfoil grows outward due to ice accumulation, with the majority of the ice concentrated at the leading edge. Areas outside the droplet impact limits experience minimal icing. As the temperature rises, part of the water on the airfoil surface freezes while some overflows, resulting in a distinct ice angle; at this point, the icing is classified as glaze ice.

To assess the accuracy of the icing calculation method used in this study, we compared our results with the actual ice shape measurements from Shin et al. [36] conducted at NASA IRT, as well as with the ice shape calculations from the LEWICE software [37] under identical conditions.

The cross-sectional position of the ice shape was chosen at the midpoint of the wing span, as indicated by the black line in Fig. 11(a). The coordinates were normalized by dividing both the x and y coordinates by the chord length.

Figure 12(a) shows the predicted ice shape on the NACA0012 airfoil after 6 minutes of icing at -19.4°C. Owing to the relatively low ambient temperature, this condition corresponds to rime ice accretion. As shown in the figure, the present prediction agrees well with the experimental ice shape in terms of the maximum ice thickness and the icing limit on the lower surface. The relative error in the maximum ice thickness with respect to the experimental result is 1.32%. However, compared with the experimental ice shape, the predicted ice shape on the upper surface is still slightly larger. Overall, the present icing calculation method demonstrates good predictive capability for rime-ice accretion. Compared with the LEWICE result, the predicted ice surface obtained in this study is slightly less smooth, which is likely related to local errors in the calculation of the convective heat transfer coefficient induced by the mesh, thereby causing certain differences in the predicted ice accretion at different locations.

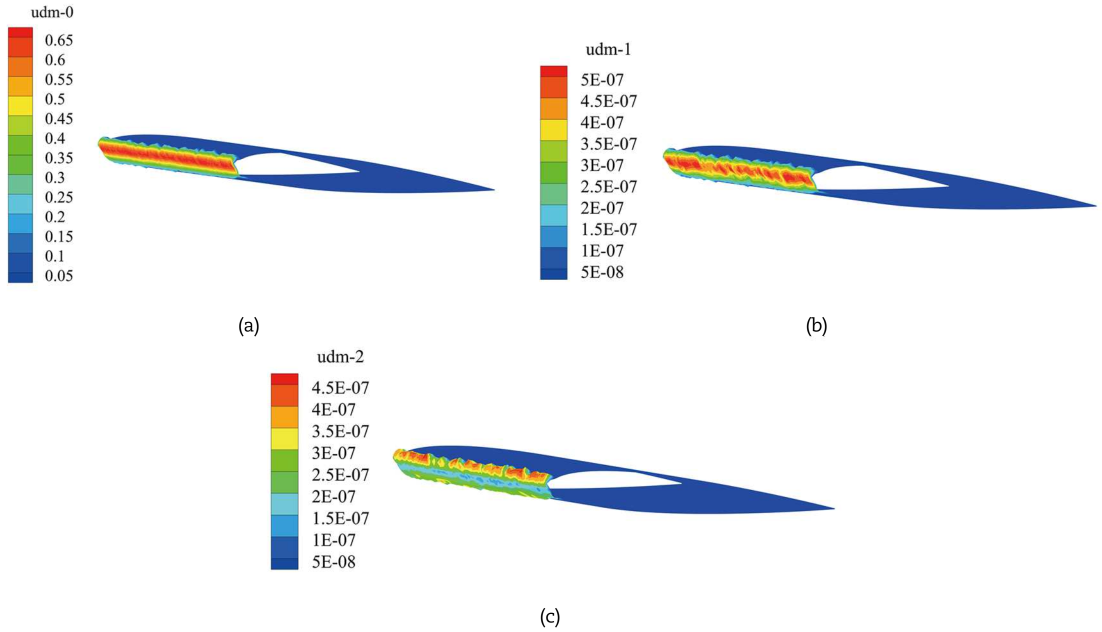

Fig. 13. Contour distributions of characteristic icing-related parameters on the NACA0012 airfoil surface under glaze-ice conditions at −10°C, (a) Local water collection coefficient, (b) Droplet impingement mass flow rate (kg/s), and (c) Ice accretion mass flow rate (kg/s). The results show that droplet impingement is mainly concentrated near the leading edge, whereas the ice accretion region extends further along the upper surface due to runback water transport.

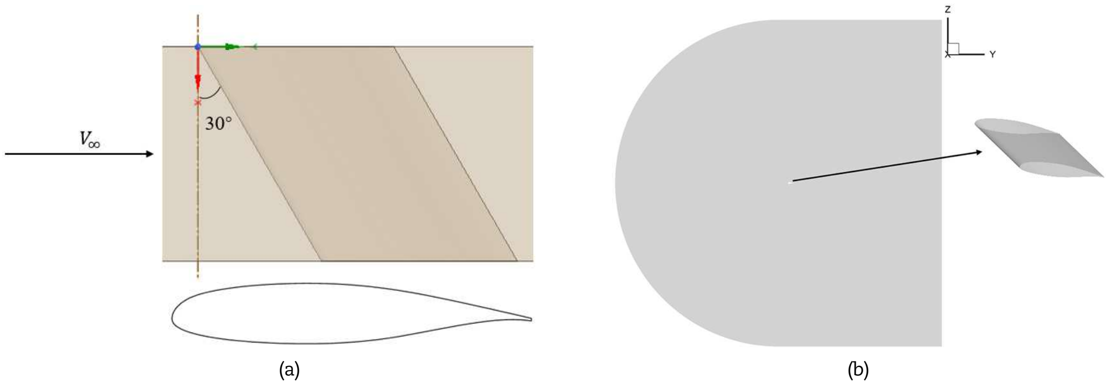

Fig. 14. Computational model of MS-317, (a) Schematic of the computational profile, (b) Computational domain model.

Figure 12(b) presents the comparison results for the glaze-ice condition. It can be seen that the predicted upper and lower icing limits are generally consistent with the experimental ice shape, with a discrepancy of about 2.3%, and the location of the ice horn is also in close agreement with the experimental result. Compared with the LEWICE result, the present method provides a more accurate prediction of the maximum ice thickness. The main discrepancy is that the predicted ice thickness on the lower surface is relatively larger, suggesting that part of the unfrozen water in the computation runs back to the lower surface to a greater extent, leading to a deviation from the experimental result.

At -10°C, the cloud maps of the local water collection coefficient, droplet impingement mass flow rate, and ice accretion mass flow rate on the airfoil surface are shown in Fig. 13. In the figure, udm-0, udm-1, and udm-2 represent custom memory spaces in Fluent, storing the local water collection coefficient, droplet impingement mass flow rate, and ice accretion mass flow rate on the airfoil surface, respectively. The color scale indicates that red represents larger values, while blue indicates smaller values.

From the local water collection coefficient cloud map (see Fig. 13(a)), it is evident that the distribution of the droplet collection coefficient is relatively uniform, primarily concentrated at the leading edge of the airfoil. Outside the impact limit range, the values approach zero. The distribution range of the droplet impingement mass flow rate closely aligns with that of the collection coefficient; however, the continuity of the droplet impingement mass flow rate distribution is lower than that of the collection coefficient (see Fig. 13(b)). This may be attributed to the movement of the mesh during each icing time step, which alters the mesh area and causes the mesh to become less uniform compared to a smooth airfoil surface, resulting in decreased continuity.

The distribution of ice accretion mass flow rate on the airfoil surface clearly illustrates that water has overflowed from the original impact location to the upper surface of the airfoil (see Fig. 13(c)). This is evidenced by the distinct ice angle, which is more pronounced in glaze ice compared to rime ice. Furthermore, the ice accretion mass flow rate is smaller than the droplet impingement mass flow rate due to some water evaporation.

The analysis above demonstrates the effectiveness of the icing model calculation method used in this study and the rationality of the runback water distribution.

5.3. Validation of ice shapes on MS-317

The second icing verification model is the MS-317 swept wing, with a sweep angle of 30°. The cross-section of the airfoil along the flow direction is the same MS-317 airfoil, with a chord length of 0.9144 m. The geometry and computational domain are illustrated in Fig. 14.

Table 5. MS-317 Icing calculation parameters.

Serial Number	Free stream temperature (°C)	Ice accretion time (s)	LWC (g/m³)	MVD (μm)	Free stream velocity (m/s)
1	-17.8	1164	1.03	20	67.056
2	-17.8	390	1.03	20	67.056
3	-2.2	1164	1.03	20	67.056
4	-2.2	390	1.03	20	67.056

Table 6. Grid independence analysis for the MS-317 icing case.

Mesh level	Number of cells	Maximum ice thickness (mm)	Absolute relative change to next finer mesh (%)
G1	2.00M	12.0	23.33
G2	2.80M	9.2	11.96
G3	3.58M	8.1	1.23
G4	4.52M	8.2	-

Four operating conditions were selected for computational validation, featuring different temperatures and icing durations, with an angle of attack of 8°. The detailed parameters are presented in Table 5.

The computational mesh and pressure-field distribution for the MS-317 case are shown in Fig. 15. Local mesh refinement was applied near the airfoil surface to improve the resolution of the icing surface and the accuracy of subsequent droplet impingement and ice accretion calculations. A grid independence study was also carried out for this case under the inflow conditions of Condition 2 in Table 5, and the corresponding results are listed in Table 6. Four mesh levels were examined, and the predicted maximum ice thicknesses were 12.0, 9.2, 8.1, and 8.2 mm, respectively. The absolute relative changes between two consecutive mesh levels were 23.33%, 11.96%, and 1.23%, respectively. Considering the small variation in maximum ice thickness between the two finest meshes, the mesh with 3,577,793 cells was finally adopted for the subsequent simulations as a balance between computational accuracy and efficiency. The incoming flow velocity was directed along the positive y-axis.

Figure 16 shows the ice formation on the MS-317 validation model at a temperature of -17.8°C. Two icing durations were computed: 1164 seconds and 390 seconds. The icing time steps were set at 300 seconds and 120 seconds, with a total of four updates conducted. From Fig. 16, it can be seen that the icing thickness increases significantly with the passage of time. Additionally, the ice shape at the wingtip is irregular, while the rest of the surface remains relatively smooth. This irregularity may be attributed to the higher distortion rate of the mesh at the endpoints, leading to computational errors. To compare the results with those from literature [38] and experimental results from literature [39], the cross-sectional ice shape at the midpoint of the wing span is selected, as indicated by the line in Fig. 16(a), and the comparisons are shown in Fig. 17.

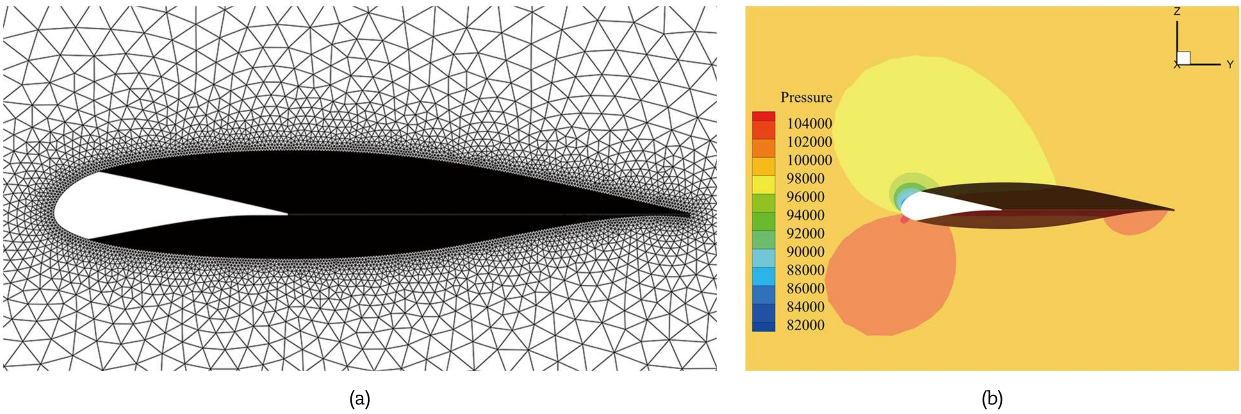

Fig. 15. Computational mesh and pressure-field distribution for the MS-317 swept-wing case, (a) Mesh generation with local refinement on the wing surface, and (b) Pressure contour in the computational domain. The pressure legend is given in Pa.

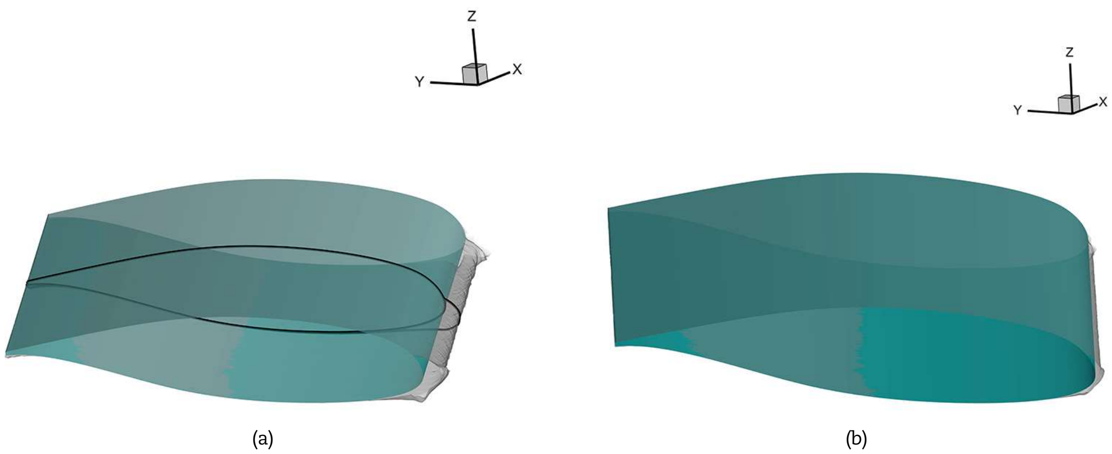

Fig. 16. Icing conditions on MS-317 airfoil surface at -17.8°C, (a) Ice shape at icing time of 1164 s, (b) Ice shape at icing time of 390 s.

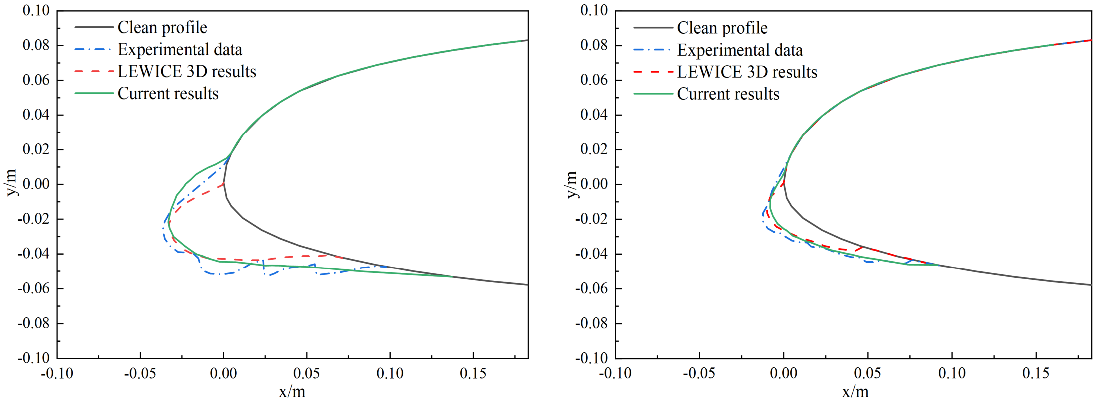

(a) (b)

Fig. 17. Comparison of ice shapes on MS-317 airfoil surface at -17.8°C, (a) Ice accretion time of 1164 s, (b) Ice accretion time of 390 s.

(a) (b)

Fig. 18. Icing conditions on MS-317 airfoil surface at -2.2°C, (a) Ice shape at ice accretion time of 1164 s, (b) Ice shape at ice accretion time of 390 s.

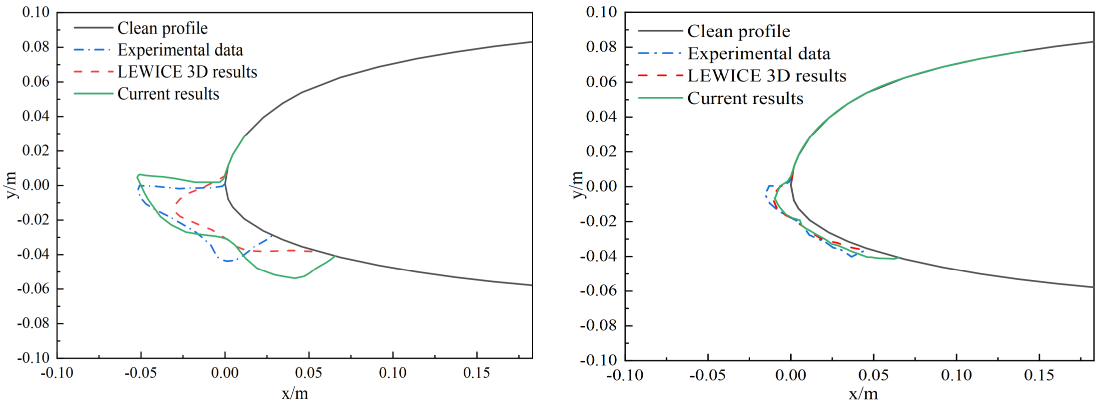

(a) (b)

Fig. 19. Comparison of ice shapes on MS-317 airfoil surface at -2.2°C, (a) Ice accretion time of 1164 s, (b) Ice accretion time of 390 s.

The results show that, under the rime-ice condition, the present prediction is in good agreement with the experimental ice shape in terms of both the icing limits and the overall ice profile. The upper and lower icing limits are slightly overestimated, while the predicted maximum ice thickness is slightly smaller than both the experimental result and the LEWICE 3D prediction, with an error of approximately 8.4% relative to the experimental value. In addition, the experimental ice shape on the lower surface exhibits irregular fluctuations, which are not reproduced in the present simulation. Nevertheless, the overall predicted ice profile remains generally consistent with the experimental result.

During the calculations, some negative mesh occurrences were noted due to prolonged icing time. The approach taken was to export the ice shape at that time step, rebuild the computational domain, and redefine the mesh, then sequentially solve until the target time was reached.

Figure 18 illustrates the ice formation at a temperature of -2.2°C, with icing durations of 1164 seconds and 390 seconds. Due to the temperature being close to 0°C, not all droplets that impacted the airfoil surface froze, some overflowed, resulting in glaze ice formation. Fig. 18 shows that as the temperature increases, there are significant changes in the ice shape. Droplet overflow has led to the formation of two ice horns, and the thickness increases with longer icing durations. The ice shape is not as smooth as at lower temperatures.

The comparison of the ice shape at the mid-span section of the airfoil with the results reported in [38, 39] is shown in Fig. 19. At an icing duration of 1164 s, the present prediction agrees well with the experimental ice shape in terms of the maximum ice thickness, with a relative error of approximately 1.87%. The ice profile on the upper surface is also relatively close to the experimental result. However, more runback water is predicted on the lower surface, resulting in a relatively large deviation in the icing limit, with an error of about 33%. At an icing duration of 390 s, certain deviations from the experimental result remain in both the maximum ice thickness and the icing limit, whereas the present prediction is closer to the LEWICE 3D result.

This discrepancy may be related to the larger amount of runback water under relatively high-temperature conditions. In the present icing model, when none of the droplets within the control volume freezes ($f \le 0$), all of the liquid water is assumed to flow out, whereas in reality part of the water may still remain on the surface. As a result, the predicted icing limit is slightly larger than that observed in the experiment, and the deviation tends to increase with icing duration.

Overall, the above results indicate that the present icing method achieves relatively high accuracy under rime-ice conditions, with both the icing limits and the maximum ice thickness showing good agreement with the experimental results. When the temperature increases to glaze-ice conditions, the present method still performs well in predicting the maximum ice thickness and the overall ice profile, whereas the prediction of the icing limits still needs further improvement. For long-duration glaze-ice conditions, the current method is still unable to provide sufficiently accurate simulations.

These limitations may arise from two aspects. First, the existing icing model is still not sufficiently complete, and the underlying icing mechanisms require further investigation. Second, the time step used in the current multi-step approach remains relatively large, so the calculation is essentially quasi-steady rather than real-time, which may further limit the prediction accuracy under prolonged glaze-ice conditions.

6. Conclusion and Future Work

A three-dimensional numerical framework for aircraft wing ice accretion has been developed on the Fluent platform. In this framework, droplet impingement characteristics are calculated using an Eulerian droplet model solved through the user-defined scalar (UDS) approach, while runback water distribution and dynamic ice-shape reconstruction are implemented on unstructured surface grids. The method has been validated using the NACA0012 straight wing and the MS-317 swept wing under representative icing conditions. The main conclusions are summarized as follows.

(1) An Eulerian droplet impingement method suitable for three-dimensional wing icing simulation was established within the Fluent framework. By distinguishing impingement and non-impingement regions according to the droplet velocity and wall-normal vector, the local water collection coefficient on complex three-dimensional surfaces can be obtained effectively. In addition, the introduction of a numerical diffusion term improves the robustness of the droplet-phase calculation. For the NACA0012 case, the predicted local water collection coefficient agrees well with the reference data, with an error of less than 1.6% near the leading edge.

(2) Based on the classical Messinger thermodynamic icing model, a runback water distribution method applicable to unstructured surface grids was developed for three-dimensional icing simulation. In this method, the overflow direction is determined according to the local flow condition, and the outflow mass is distributed according to the angle between the air velocity vector and the normal vectors of grid edges. This provides a practical treatment for three-dimensional runback water transport without relying on explicit stagnation-point detection.

(3) A three-dimensional ice-shape reconstruction and mesh deformation method was further developed using Fluent's dynamic mesh technique. By introducing area-weighted evaluation of nodal ice thickness and growth direction, the present method enables multi-step simulation of ice accretion and geometric updating on complex wing surfaces, thereby forming an integrated numerical framework from droplet impingement calculation to ice accretion prediction and ice-shape reconstruction.

(4) Validation results for the NACA0012 and MS-317 cases demonstrate that the proposed method achieves good predictive capability for rime-ice accretion. For the NACA0012 airfoil, the error in maximum ice thickness is 1.32% under rime-ice conditions, while for the MS-317 swept wing the corresponding error is about 8.4%. Under glaze-ice conditions, the present method can still predict the main ice profile and maximum ice thickness with reasonable accuracy. For the NACA0012 airfoil, the deviation in icing limit is about 2.3%. For the MS-317 swept wing at an icing duration of 1164 s, the error in maximum ice thickness is about 1.87%, although the deviation in icing limit remains relatively large at about 33%. These results indicate that the present framework is effective for predicting rime ice and can also capture the main ice-thickness and profile characteristics under glaze-ice conditions.

Overall, the present framework provides a practical numerical tool for three-dimensional wing icing simulation with runback water effects under typical aerodynamic and thermodynamic conditions. At the same time, several limitations still remain. First, under glaze-ice conditions, especially for long-duration icing cases, the current method still shows limited accuracy in predicting the icing limit. This suggests that the present treatment of unfrozen water transport and surface retention is not yet sufficiently complete. Second, the current multi-step strategy still uses relatively large time steps and is essentially quasi-steady rather than fully transient, which may further limit the accuracy of long-duration glaze-ice prediction.

Future work will therefore focus on the following aspects. First, the physical modeling of runback water motion will be further improved, especially under conditions involving strong surface water retention and complex glaze-ice formation. Second, the prediction capability for icing limits under high-temperature and long-duration icing conditions will be enhanced. Third, more efficient dynamic mesh updating and time-dependent solution strategies will be explored in order to improve both computational efficiency and physical fidelity in three-dimensional transient icing simulations.

Author Contributions

B. Yu conceived the overall study design, initiated the project, and implemented the methods and code; L. Zhang proposed the original idea and provided key conceptual guidance; C. Zhou curated the data and performed statistical analyses; Y. Lyu contributed to visualization and figure preparation and assisted with result interpretation; Z. Liu supervised the study and coordinated manuscript revision. The manuscript was written through the contribution of all authors. All authors discussed the results, reviewed, and approved the final version of the manuscript.

Acknowledgments

The authors are very grateful for the reviewers' comments and the editors' recommendations, which have helped improve the quality and presentation of this manuscript. We are thankful to the management of Northwestern Polytechnical University for their support and continuous encouragement for the present work.

Conflict of Interest

The authors declared no potential conflicts of interest concerning the research, authorship, and publication of this article.

Funding

The authors received no financial support for the research, authorship, and publication of this article.

Data Availability Statements

The datasets generated and/or analyzed during the current study are available from the corresponding author on reasonable request.

Nomenclature

α	volume fraction of the droplets	ρ_d	Density of the supercooled droplets [kg/m^3]
D	Diameter of the supercooled droplets [m]	$\mathbf{u}_d$	Velocity vector of the droplets
$\mathbf{u}_a$	Velocity vector of the air	$\mathbf{g}$	Gravitational acceleration
K	Air-droplet momentum exchange coefficient	μ_a	Dynamic viscosity of air
C_D	Drag coefficient	LWC	Liquid water content
MVD	Median volume diameter		

References

[1] Wu, J., Xu, Q., Wu, F., Xia, Q., Xu, Q., Li, S., Droplet collection efficiency regularity of NACA0012 airfoil based on the Eulerian method, *Aerospace*, 10, 2023, 412.
[2] Morency, F., Beaugendre, H., Baruzzi, G.S., Habashi, W.G., FENSAP-ICE: A comprehensive 3D simulation system for in-flight icing, *15th AIAA Computational Fluid Dynamics Conference*, Anaheim, CA, USA, AIAA Paper 2001-2566, 2001.
[3] Cao, Y., Wu, Z., Su, Y., Xu, Z., Aircraft flight characteristics in icing conditions, *Progress in Aerospace Sciences*, 74, 2015, 62-80.
[4] Papadakis, M., Yeong, H.-W., Shimoi, K., Wong, S.-H., Ice shedding experiments with simulated ice shapes, *1st AIAA Atmospheric and Space Environments Conference*, San Antonio, TX, USA, AIAA Paper 2009-3972, 2009.
[5] Cao, Y., Huang, J., Yin, J., Numerical simulation of three-dimensional ice accretion on an aircraft wing, *International Journal of Heat and Mass Transfer*, 92, 2016, 34-54.
[6] Cao, Y., Tan, W., Wu, Z., Aircraft icing: An ongoing threat to aviation safety, *Aerospace Science and Technology*, 75, 2018, 353-385.
[7] Liu, Q., Bashir, M., Huang, H., Miao, W., Xu, Z., Yue, M., Li, C., Nature-inspired innovative platform designs for optimized performance of floating vertical axis wind turbines, *Applied Energy*, 380, 2025, 125120.
[8] Ruff, G.A., Berkowitz, B.M., User's Manual for the NASA Lewis Ice Accretion Prediction Code (LEWICE), NASA CR-185129, 1990.
[9] Wright, W.B., Validation results for LEWICE 3.0, *43rd AIAA Aerospace Sciences Meeting and Exhibit*, Reno, NV, USA, AIAA Paper 2005-1243, 2005.
[10] Gent, R.W., Dart, N.P., Cansdale, J.T., Aircraft icing, *Philosophical Transactions of the Royal Society A*, 358, 2000, 2873-2911.
[11] Bourgault, Y., Beaugendre, H., Habashi, W.G., Development of a shallow-water icing model in FENSAP-ICE, *Journal of Aircraft*, 37, 2000, 640-646.
[12] Hu, L., Zhu, X., Hu, C., Chen, J., Du, Z., Calculation of the water droplets local collection efficiency on wind turbine blades, *Journal of Energy Resources Technology*, 139, 2017, 051211.
[13] Han, H., Yin, Z., Ning, Y., Liu, H., Development of a 3D Eulerian/Lagrangian aircraft icing simulation solver based on OpenFOAM, *Entropy*, 24, 2022, 1365.
[14] Messinger, B.L., Equilibrium temperature of an unheated icing surface as a function of air speed, *Journal of the Aeronautical Sciences*, 20, 1953, 29-42.
[15] Al-Khalil, K.M., Keith, T.G., DeWitt, K.J., New concept in runback water modeling for anti-iced aircraft surfaces, *Journal of Aircraft*, 30, 1993, 41-49.
[16] Myers, T.G., Thompson, C.P., Modeling the flow of water on aircraft in icing conditions, *AIAA Journal*, 36, 1998, 1010-1013.
[17] Rothmayer, A.P., Tsao, J.C., Water film runback on an airfoil surface, *38th AIAA Aerospace Sciences Meeting and Exhibit*, Reno, NV, USA, AIAA Paper 2000-0237, 2000.
[18] Dong, Y., Guo, Y., Xu, C., Yu, X., Investigation on heat transfer characteristics of aircraft icing including runback water, *International Journal of Heat and Mass Transfer*, 53, 2010, 3702-3707.
[19] Dong, W., Zheng, M., Zhu, J., Lei, G., Calculation and analysis of runback water flow on anti-icing airfoil surfaces, *Journal of Aircraft*, 53, 2016, 1597-1605.
[20] Zheng, M., Dong, W., Guo, Z., Lei, G., Analysis of runback water flow on anti-icing surfaces using the volume-of-fluid method, *ASME Turbo Expo 2017: Turbomachinery Technical Conference and Exposition*, Charlotte, NC, USA, V05AT20A003, 2017.
[21] Gao, L., Liu, Y., Hu, H., An experimental investigation of dynamic ice accretion process on a wind turbine airfoil model considering various icing conditions, *International Journal of Heat and Mass Transfer*, 133, 2019, 930-939.
[22] Wang, H., Liu, Y., Bao, C., Kai, G., Baoyin, H., Experimental and numerical study on icing characteristics of integrated wind turbines under operating conditions, *Cold Regions Science and Technology*, 246, 2026, 104846.
[23] Yang, P., Li, H., Chen, J., Duan, Y., Zhang, Y., Influence of airflow field computation on ice accretion simulation of airfoils, *Aerospace Science and Technology*, 151, 2024, 109315.
[24] Hospers, J., Hoeijmakers, H.W.M., Numerical method for ice accretion on three-dimensional wings, *28th ICAS Congress*, 2012, 802-808.
[25] Donizetti, A., Bellosta, T., Guardone, A., Ice shape convergence in multi-step ice accretion simulations over straight wings, *AIAA SciTech 2024 Forum*, AIAA Paper 2024-2679, 2024.
[26] Yang, Q., Guo, X., Dong, W., Wang, A., Ice accretion and aerodynamic effects on a turbofan engine nacelle under takeoff conditions, *Aerospace Science and Technology*, 126, 2022, 107571.
[27] Bornhoft, B., Jain, S.S., Goc, K., Bose, S.T., Moin, P., Large-eddy simulations of the NACA23012 airfoil with laser-scanned ice shapes, *Aerospace Science and Technology*, 146, 2024, 108957.
[28] Tu, J., Tian, W., Wang, X., Tian, L., Experimental study on ice mitigation and shedding over a rotating UAV propeller with hydro-/icephobic substrates, *Aerospace Science and Technology*, 155, 2024, 109610.
[29] Tong, X., Luke, E.A., Eulerian simulations of icing collection efficiency using a singularity diffusion model, *43rd AIAA Aerospace Sciences Meeting and Exhibit*, Reno, NV, USA, AIAA Paper 2005-1246, 2005.
[30] Wirogo, S., Srirambhatla, S., An Eulerian method to calculate the collection efficiency on two- and three-dimensional bodies, *41st AIAA Aerospace Sciences Meeting and Exhibit*, Reno, NV, USA, AIAA Paper 2003-1073, 2003.
[31] Yang, S., Lin, G., Shen, X., Numerical computation of droplet impingement characteristics on complex three-dimensional surfaces, *Journal of Aerospace Power*, 25, 2010, 284-290.
[32] Yang, S., Lin, G., Numerical simulation of the wing icing process, *Journal of Aerospace Power*, 26, 2011, 323-330.
[33] Shen, X., Lin, G., Bu, X., Yu, J., Hou, P., Three-dimensional numerical simulation of ice accretion on the inlet nacelle leading edge of aero-engines, *Acta Aeronautica et Astronautica Sinica*, 34, 2013, 517-524.
[34] Bidwell, C.S., Mohler, S.R., Jr., Collection Efficiency and Ice Accretion Calculations for a Sphere, a Swept MS(1)-317 Wing, a Swept NACA-0012 Wing Tip, an Axisymmetric Inlet, and a Boeing 737-300 Inlet, NASA TM-106831, AIAA Paper 95-0755, 1995.
[35] Zhu, J., *Numerical Methods for Flow and Heat Transfer in Aircraft Anti-Icing and Icing Processes*, Ph.D. Thesis, Shanghai Jiao Tong University, Shanghai, China, 2020.
[36] Shin, J., Bond, T.H., Results of an icing test on a NACA 0012 airfoil in the NASA Lewis Icing Research Tunnel, *30th AIAA Aerospace Sciences Meeting and Exhibit*, AIAA Paper 92-0647, 1992.
[37] Shin, J., Bond, T.H., Experimental and Computational Ice Shapes and Resulting Drag Increase for a NACA 0012 Airfoil, NASA TM-105743, 1992.
[38] Potapczuk, M.G., Bidwell, C.S., Numerical Simulation of Ice Growth on a MS-317 Swept Wing Geometry, NASA TM-103705, AIAA Paper 91-0263, 1991.
[39] Bidwell, C.S., Icing Characteristics of a Natural-Laminar-Flow, a Medium-Speed, and a Swept, Medium-Speed Airfoil, NASA TM-103693, AIAA Paper 91-0447, 1991.

ORCID iD

Bangtuo Yu https://orcid.org/0009-0006-3339-6226
Lifen Zhang https://orcid.org/0009-0004-0151-924X
Chengxin Zhou https://orcid.org/0009-0009-5833-2263
Yaguo Lyu https://orcid.org/0000-0003-2336-0503
Zhengang Liu https://orcid.org/0000-0002-5341-8828

How to cite this article: Yu B., et al., Three-Dimensional Numerical Simulation of Aircraft Wing Ice Accretion Using an Eulerian Droplet Model with Runback Water Distribution, *J. Appl. Comput. Mech.*, xx(x), 2026, 1–17. https://doi.org/10.22055/jacm.2026.49171.5779